Article

Synthesis, Structural and Magnetic Characterization of Superparamagnetic $Ni_{0.3}Zn_{0.7}Cr_{2-x}Fe_xO_4$ Oxides Obtained by Sol-Gel Method

Abdulrahman Mallah [1,*] , **Fatimah Al-Thuwayb** [1], **Mohamed Khitouni** [1], **Abdulrahman Alsawi** [2], **Joan-Josep Suñol** [3] , **Jean-Marc Greneche** [4] and **Maha M. Almoneef** [5]

1 Department of Chemistry, College of Science, Qassim University, Buraydah 51452, Saudi Arabia; 411207168@qu.edu.sa (F.A.-T.); kh.mohamed@qu.edu.sa (M.K.)
2 Department of Physics, College of Science, Qassim University, Buraydah 51452, Saudi Arabia; ansaoy@qu.edu.sa
3 Department of Physics, University of Girona, Campus Montilivi, 17071 Girona, Spain; joanjosep.sunyol@udg.edu
4 Institut des Molécules et Matériaux du Mans (IMMM), UMR CNRS 6283, Université du Maine, Avenue Olivier Messiaen, CEDEX 9, 72085 Le Mans, France; jean-marc.greneche@univ-lemans.fr
5 Physics Department, Faculty of Science, Princess Nourah bint Abdulrahman University, Riyadh 11564, Saudi Arabia
* Correspondence: a.mallah@qu.edu.sa; Tel.: +966-163-012-507

Abstract: The sol-gel process was used to produce ferrite $Ni_{0.3}Zn_{0.7}Cr_{2-x}Fe_xO_4$ compounds with x = 0, 0.4, and 1.6, which were then subsequently calcined at several temperatures up to 1448 K for 48 h in an air atmosphere. X-ray diffraction (XRD), scanning electron microscopy (SEM), vibrating sample magnetometer (VSM), and ^{57}Fe Mössbauer spectrometry were used to examine the structure and magnetic characteristics of the produced nanoparticles. A single-phase pure $Ni_{0.3}Zn_{0.7}Cr_{2-x}Fe_xO_4$ nanoparticle had formed. The cubic $Fd3m$ spinel structure contained indexes for all diffraction peaks. The crystallite size is a perfect fit for a value of 165 ± 8 nm. Based on the Rietveld analysis and the VSM measurements, the low magnetization Ms of $Ni_{0.3}Zn_{0.7}Cr_{2-x}Fe_xO_4$ samples was explained by the absence of ferromagnetic Ni^{2+} ions and the occupancy of Zn^{2+} ions with no magnetic moments in all tetrahedral locations. Moreover, because of the weak interactions between Fe^{3+} ions in the octahedral locations, the magnetization of the current nanocrystals is low or nonexistent. According to Mössbauer analyses, the complicated hyperfine structures are consistent with a number of different chemical atomic neighbors, such as Ni^{2+}, Zn^{2+}, Cr^{3+}, and Fe^{3+} species that have various magnetic moments. A Fe-rich neighbor is known to have the highest values of the hyperfine field at Fe sites, while Ni- and Cr-rich neighbors are responsible for the intermediate values and Zn-rich neighbors are responsible for the quadrupolar component.

Keywords: sol-gel method; ferrite oxides; superparamagnetic

1. Introduction

Due to a remarkable combination of their outstanding physical, chemical, and structural features, as well as a variety of promising applications, mixed ferrite systems have attracted increasing attention in recent years. Due to their significant magnetic properties, particularly in the radio frequency region, physical flexibility, high electrical resistivity, mechanical hardness, and chemical stability, spinel ferrites are among an important class of magnetic materials [1–8]. The majority of mixed oxides, except the lithium-nickel oxide and the lithium-cobalt oxide systems, possess a spinel structure of the general formula $M_xM'_{3-x}O_4$ (M, M' = Ni, Co, Fe, Mn, Cr...). Thirty-two oxygen atoms are arranged between tetrahedral (A) and octahedral (B) sites in a cubic closed-packed arrangement that makes up the unit cell of spinel ferrites.

The compositions and synthesis methods of spinel ferrite nanostructures have an impact on their chemical and structural characteristics, and the cation substitutions determine the corresponding electric and magnetic properties. In ferrites, whose crystal chemical formula is $(M^{2+}_{1-x}Fe^{3+}_x)_{tetra}(M^{2+}_x Fe^{3+}_{2-x})_{octa} O_4$ [9], a specific cationic distribution is allowed. The "degree of inversion", denoted by the letter "x", corresponds to the fraction of sites (A) that are occupied by Fe^{3+} cations. Two extreme examples associated with the change of the cation configuration can be distinguished. One is the standard spinel (x = 0), which has all Fe^{3+} cations in the (B) locations and all M^{2+} cations in the (A) locations. The other is an inverse spinel (x = 1), where the M^{3+} cations are distributed equally in the A and B sites and all M^{2+} ions occupy the (B) regions. It is also quite common to find spinels that have a somewhat inverse cation distribution, which falls in between normal and inverse spinels (0 < x < 1).

The features of spinel ferrites are greatly influenced by the cation distribution, which is connected to the process of elaboration [10]. Furthermore, when the particle size is in the nanometer range, it has a noticeable impact on the physical and chemical characteristics of ferrite and other magnetic materials. High surface-to-volume ratio nanoparticles show noticeable magnetic properties in comparison to their massive counterparts [11–13]. With the reduction in grain size, ferrite nanoparticles exhibit characteristics such as high field irreversibility [14], change in Neel temperature [15], higher coercivity values [16], lower saturation magnetization values, modified lowered, or increased magnetic moments [17–19], etc. Among the ferrites that are an important component of magnetic ceramic materials, nanosized nickel ferrite, $NiFe_2O_4$, has desirable characteristics for use as soft magnets due to its high electrical resistivity, low coercivity, and low saturation magnetization values. These qualities make it a suitable material for magnetic and magneto-optical applications. Nanostructured $NiFe_2O_4$ is a great core material for power transformers in electronics and communication systems, since it has nearly no hysteresis losses [20,21]. In addition, $NiFe_2O_4$ nanoparticles are well known for their use in electrical, electronic, and catalytic applications, as well as for their ability to sense gases and humidity [22]. It has been noted that the magnetic properties of $NiFe_2O_4$ are significantly influenced by the size of the crystallite. For bulk systems, the impact of the structure on the magnetic characteristics of $NiFe_2O_4$ has been demonstrated [23,24].

According to Brook and Kingery [25], depending on their structure, $NiFe_2O_4$ samples display ferrimagnetism, superparamagnetism, or paramagnetism. In actuality, superparamagnetism is associated with materials with grains smaller than 10 nm, and ferrimagnetism is associated with samples with grains larger than 15 nm, while paramagnetism is related to the non-crystalline (or amorphous) materials that might resemble a totally disordered state. In contrast to their bulk counterpart, $NiFe_2O_4$ nanoparticles exhibit higher coercivity and lower saturation magnetization values [26–29]. The magnetic properties of $NiFe_2O_4$ result in the super-exchange interactions between the tetrahedral and octahedral sublattices as the metallic ions are surrounded by oxygen atoms. In addition, the magnetic properties are also influenced by the magnetocrystalline anisotropy, the canting effect resulting from the presence of triangular cationic platelets and antiferromagnetic interactions, and the dipolar interactions between projected moments on the nanoparticle surface. To improve some of their electric or magnetic properties, ferrite nanocrystals can be doped with several metallic species, including chromium, copper, manganese, and zinc [30–32]. For instance, they noted that the Cu replacement in NiZn-ferrite increases permeability, saturation magnetization, and magnetic losses; tan δ (dielectric losses) at 1.3 GHz is <0.01 in NiCuZn, but it is substantially lower (6×10^{-3}) in NiZn [33,34]. On the other hand, cations such as Cr^{3+}, in particular, show a significant predilection for substituting into the B-site and a tendency for anti-ferromagnetic coupling with Fe. This causes magnetic fluctuations in the system, resulting in interesting magnetic characteristics when one of the cations is partially or completely substituted with Cr^{3+}. As a result, it is interesting to investigate its magnetic properties with Cr in place of Fe, which is expected to change the frustration in the system [35–37]. Sijo et al. [38] investigated the impact of the Cr substitution on the

structural, magnetic, and dielectric properties in $NiCrFeO_4$ nanoparticles prepared by the solution combustion method. Because of the distribution of cations between the tetrahedral A and octahedral B-sites, $NiCrFeO_4$ exhibited significant changes in its atomic arrangement depending critically on preparation temperature. B-sites are where chromium ions chose to concentrate. Ni^{2+} and Fe^{3+} were distributed differently between octahedral and tetrahedral sites as a result of temperature, which had an impact on their characteristics and material properties. They noticed that substituting one Cr cation for one Fe cation in $NiFe_2O_4$ decreased the transition temperature. Furthermore, their Mössbauer investigations at room temperature showed the presence of small superparamagnetic particles and larger-sized ferrimagnetic particles. On the other hand, while spinel ferrites can be made using a variety of processes, the sol-gel method produces high-purity, nanocrystalline, and homogeneous ferrites, which have an important influence on the structural and magnetic properties.

In this work, we have studied the impact of Cr substitutions on nickel, zinc, and ferrite nanocrystalline structures produced by the sol-gel method. At ambient temperature, we specifically describe the structural and magnetic characteristics of these doped materials. In addition, we have examined in detail the Mössbauer spectra of the doped samples.

2. Materials and Methods

2.1. Preparation Method

Due to its rapid reaction rate, low preparation temperature, and generation of tiny particles, the sol-gel method is frequently utilized in the synthesis of ferrite nanocrystals. Mixed oxides were prepared by this method based on the Pechini procedure utilizing stoichiometric proportions of the precursors' $Ni(NO_3)_2 6H_2O$, $Zn(NO_3)_2 6H_2O$, $Fe(NO_3)_3 9H_2O$, and $Cr(NO_3)_3 9H_2O$. Thus, in our experiment, nanocrystalline $Ni_{0.3}Zn_{0.7}Cr_{2-x}Fe_xO_4$ with x = 0, 0.4, and 1.6 were synthesized by this method. To create a mixed solution, stoichiometric proportions of metal nitrates were first fully dissolved in distilled water. Then, as a chelating agent, measured quantities of citric acid were added and dissolved while stirring. The molar ratio of nitrates to citric acid was set to 1:1, and a little amount of ammonia solution was added to the mixture to change the pH to 7. Ethylene glycol was then added as a polymerization agent after the solution had been heated to 373 K while being stirred. Until the gel was obtained, the heating was continued. The produced wet gel was dried to obtain a dry foam, which was then milled in a mortar; then each sample was heated in air atmosphere at 473 K for 24 h, 773 K for 24 h, 973 K for 24 h, 1173 K for 24 h and finally at 1448 K for 48 h to achieve the desired crystalline phase. All samples were milled after each heat process.

2.2. Measurements and Characterizations

Using a Philips® PW1800 X-ray diffractometer with CuKα radiation (λ = 1.54056 Å) operating at 40 kV and 30 mA, X-ray diffraction patterns (XRD) of the produced nanocrystals were obtained. The Rietveld refinement method was applied with Fullprof software [39]. A Hitachi® S4160 Field Emission Scanning Electron Microscope (FE-SEM) was used to examine the samples' morphology and average particle size. Meghnatis Daghigh Kavir Co.® Vibrating Sample Magnetometer (VSM) was used to assess the samples' magnetic characteristics while they were at room temperature. A maximum magnetic field of 9 kOe was applied during these tests, it should be noted.

Following the synthesis of these nanocrystals from the precursors at the atomic level, a ^{57}Co source diffused into a rhodium matrix was used for conventional ^{57}Fe Mössbauer transmission spectrometry at 300 and 77 K. In order to describe the broadened quadrupolar and/or magnetic components, the Mössbauer spectra were fitted using the Mosfit program [40], which involved quadrupolar components and magnetic sextets with Lorentzian lines or discontinuous distribution of quadrupolar and/or magnetic sextets. The proportions of Fe species are obtained from the relative absorption area of the relevant component, assuming the same value of recoilless f-factor, while the values of isomer shift refer to that of α-Fe at room temperature.

3. Results

3.1. Structural Analyses

Figure 1 depicts the XRD diffractograms for the produced $Ni_{0.3}Zn_{0.7}Cr_{2-x}Fe_xO_4$ (x = 0; 0.4; 1.6) ferrites. In accordance with well-crystallized samples, all the XRD patterns show well-defined and relatively thin Bragg peaks. XRD patterns of all the ferrite particles present the spinel structure and are well indexed to (111), (220), (311), (222), (400), (422), (511), (440), (620), (533), (622), and (642) crystal planes of cubic spinel phase. The cubic *Fd3m* spinel structure had indexes for all diffraction peaks. Knowing the distribution of cations between the tetrahedral (A) and octahedral (B) sites is important to refine the structure of $Ni_{0.3}Zn_{0.7}Cr_{2-x}FexO_4$ samples using the Rietveld method. Using X-ray powder diffraction data, the Rietveld structural refinement was done using the FULLPROF-suite software; this is a well-established technique for extracting structural details from powder diffraction data. Measurements using the (in-field) Mössbauer spectroscopy method have been used to determine the cations distributions for ferrites with the general formula AB_2O_4. In earlier research, Mössbauer characterization of some Ni-Zn ferrites [41] and Cr-substituted ferrites [42,43] revealed that Zn^{2+} ions prefer to occupy the tetrahedral (A) regions, while Ni^{2+} ions are distributed on the octahedral (B) regions, and Fe^{3+} and Cr^{3+} ions are distributed on both sites. These cations' distribution has been verified in various investigations [44–47]. As a result, the cation distribution for the $Ni_{0.3}Zn_{0.7}Cr_{2-x}Fe_xO_4$ samples can be written as $\left(Zn_{0.7}^{2+}Cr_{0.3}^{3+}\right)_A\left[Ni_{0.3}^{2+}Cr_{1.7}^{3+}\right]_B O_4^{2-}$ (for x = 0), $\left(Zn_{0.7}^{2+}Fe_{0.3}^{3+}\right)_A\left[Ni_{0.3}^{2+}Cr_{1.6}^{3+}Fe_{0.1}^{3+}\right]_B O_4^{2-}$ (for x = 0.4), and $\left(Zn_{0.7}^{2+}Fe_{0.3}^{3+}\right)_A\left[Ni_{0.3}^{2+}Cr_{0.4}^{3+}Fe_{1.3}^{3+}\right]_B O_4^{2-}$ (for x = 1.6). The Rietveld refinement was carried out using this created formula. The atomic locations for (A) cations, (B) cations, and O were taken at positions 8a (1/8, 1/8, 1/8), 16d (1/2, 1/2, 1/2), and 32e (x, y, z).

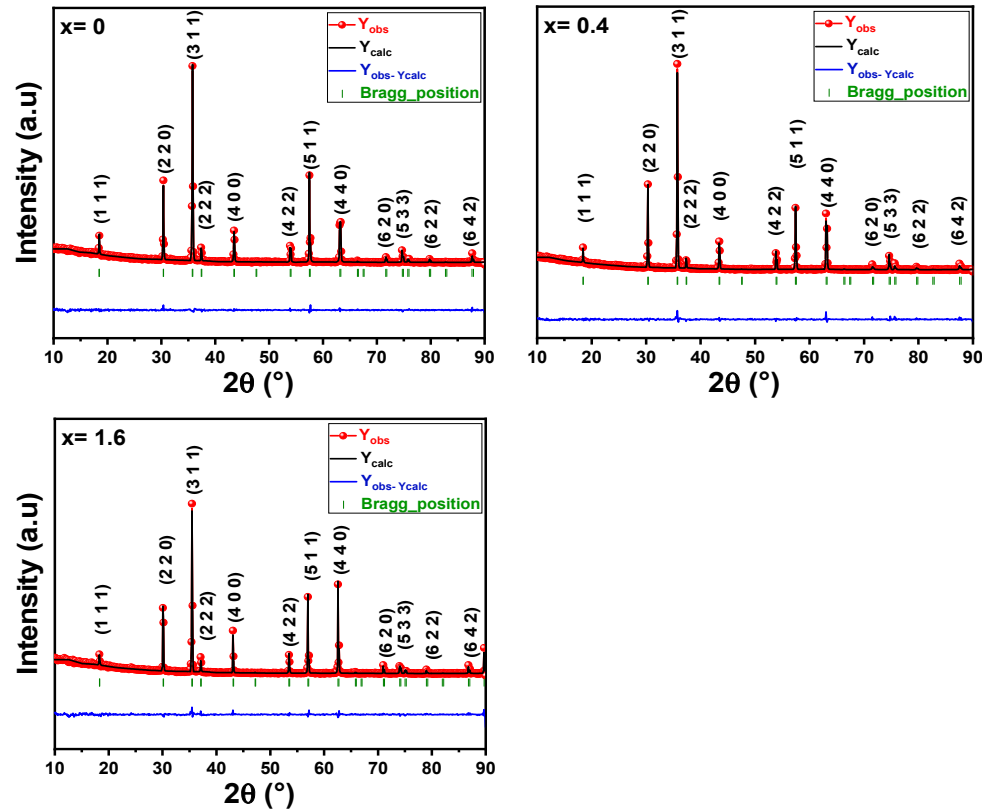**Figure 1.** XRD patterns with Rietveld refinement for $Ni_{0.3}Zn_{0.7}Cr_{2-x}Fe_xO_4$ ferrites: the bottom line (green) represents the difference between the XRD data (red) and calculated fit (black), and the blue lines represent the Bragg positions.

In the structural refinement procedure of our samples, we have followed the standard steps of the Rietveld method, which consists of following the sequence: (i) refinement of overall Scale factor + background coefficients (all other parameters are kept fixed); (ii) the same + refinement of detector zero offset (or sample displacement in Bragg-Brentano geometry) + refinement of lattice parameters; (iii) the same + refinement of shape parameters + refinement of asymmetry parameters; (iv) the same + refinement of atomic positions + refinement of global Debye-Waller parameter or thermal agitation factors; and (v) the same + refinement of site occupancy rate. In our refinements, we have taken care to respect this sequence of steps to release the different parameters. This ensures a stability of the refinement with all the parameters released. Table 1 provides the refined values for the structural parameters. Small residual values in the goodness of fit (χ^2) confirm the good agreement between the computed and observed XRD data, as seen in Figure 1. The parameters presented in Table 1 with uncertainty in brackets (such as lattice constant, cell volume, isotropic thermal agitation parameter, bond length, and bond angle) are those which are refined. The parameters presented without uncertainty (such as atomic position and occupancy factor) are those fixed.

Table 1. Structural characteristics for $Ni_{0.3}Zn_{0.7}Cr_{2-x}Fe_xO_4$ ferrites obtained following the structural refinement by the Rietveld method. B_{iso}: isotropic thermal agitation parameter. Definitions of structural parameters are given in the text. R factors: R_P = profile factor, R_B = Bragg factor, and R_F = crystallographic factor). χ^2: The goodness of fit. The numbers in parentheses are estimated standard deviations to the last significant digit.

Fe Content			x = 0	x = 0.4	x = 1.6
Space group			Fd − 3m		
Cell parameters		Lattice constant a (Å)	8.3242 (5)	8.3329 (5)	8.3906 (5)
		Cell volume V (Å³)	476.80 (6)	578.62 (6)	590.71 (6)
Atoms	Zn/Cr/Fe	Wyckoff positions	4c	4c	4c
		Site symmetry	−43 m	−43 m	−43 m
		Atomic positions x = y = z	1/8	1/8	1/8
		Occupancy factors	$\left(Zn_{0.7}^{2+}Cr_{0.3}^{3+}\right)_A$	$\left(Zn_{0.7}^{2+}Fe_{0.3}^{3+}\right)_A$	$\left(Zn_{0.7}^{2+}Fe_{0.3}^{3+}\right)_A$
		Biso (Å²)	2.2 (4)	1.9 (5)	1.98 (4)
	Ni/Fe/Cr	Wyckoff positions	16d	16d	16d
		Site symmetry	−3 m	−3 m	−3 m
		Atomic positions x = y = z	1/2	1/2	1/2
		Occupancy factors	$\left[Ni_{0.3}^{2+}Cr_{1.7}^{3+}\right]_B$	$\left[Ni_{0.3}^{2+}Cr_{1.6}^{3+}Fe_{0.1}^{3+}\right]_B$	$\left[Ni_{0.3}^{2+}Cr_{0.4}^{3+}Fe_{1.3}^{3+}\right]_B$
		Biso (Å²)	2.4 (4)	1.5 (5)	1.8 (3)
	O	Wyckoff positions	32e	32e	32e
		Site symmetry	3 m	3 m	3 m
		Atomic positions x = y= z	0.2582 (1)	0.2572 (2)	0.2558(2)
		Occupancy factors	O_4^{2-}	O_4^{2-}	O_4^{2-}
		Biso (Å²)	2.1 (5)	1.2 (8)	2.8 (7)
Structural parameters		RA (Å)	1.920 (1)	1.905 (2)	1.904 (2)
		RB (Å)	2.015 (1)	2.027 (2)	2.049 (2)
		θA-O-B (°)	122.5 (4)	122.9 (7)	123.3 (7)
		θB-O-B (°)	93.8 (4)	93.2 (7)	92.8 (7)
		Dc (nm)	156	163	172
Agreement factors		R_P (%)	6.29	6.73	7.45
		R_{wp} (%)	8.32	9.15	9.59
		R_F (%)	4.26	5.01	8.06
		χ^2 (%)	1.20	1.43	1.51

The lattice parameters rise linearly with Fe substitution, as seen in Table 1. This is explained by the Fe^{3+} ion's larger radius $r_{Fe}^{3+} = 0.67$ Å compared to the Cr^{3+} ion's smaller radius $r_{Cr}^{3+} = 0.63$ Å [48]. Additionally, the oxygen atomic locations that were determined are indicative of the spinel structure [49,50]. The computed and provided crystallite size (D_c) values in Table 1 rise from 156 nm for x = 0 to 173 nm for x = 1.6, respectively.

Additionally, as Fe^{3+} content increases in $Ni_{0.3}Zn_{0.7}Cr_{2-x}Fe_xO_4$ (x = 0; 0.4; 1.6) samples, the cation-oxygen bond length at the tetrahedral sites (R_A) decreases; however, the cation-oxygen bond length at the octahedral sites (R_B) increases. The values of the bond angles ($\theta_{A\text{-}O\text{-}B}$ and $\theta_{B\text{-}O\text{-}B}$) were also presented in Table 1 for $Ni_{0.3}Zn_{0.7}Cr_{2-x}Fe_xO_4$ samples. The $\theta_{A\text{-}O\text{-}B}$ bond angle is concerned with the A-O-B interactions, while the $\theta_{B\text{-}O\text{-}B}$ bond angle is related to the B-O-B interactions. From the data presented in Table 1, the increase in bond angle ($\theta_{A\text{-}O\text{-}B}$) with Fe^{3+} substitution indicates an increase in the strength of A-B exchange interactions, and the decrease in the bond angle ($\theta_{B\text{-}O\text{-}B}$) indicates a decrease in the strength of B-B exchange interactions [51,52].

On the other hand, it is well known that due to the crystalline size effect and intrinsic strain effect, the X-ray diffraction peak broadens in nanocrystals, and this peak broadening typically consists of two parts: instrumental broadening and physical broadening [53,54]. The following connection can be used to fix this instrumental broadening:

$$\beta_D = \left[\left(\beta_m^2 - \beta_i^2 \right)^{1/2} \times (\beta_m - \beta_i) \right]^{1/2} \tag{1}$$

where β_m is the measured broadening, β_i is the instrumental broadening, and β_D is the corrected broadening. Here, crystalline silicon has been used as a standard reference material for position calibration and instrumental broadening calculation. To estimate the crystallite size using XRD profiles, a number of models have been created, including the Halder-Wagner approach, the Williamson-Hall plot, and the Scherrer equation [55]. Using the Williamson-Hall (W-H) plot model [56,57], the average crystallite size for each studied oxide sample was determined in the current study. This model contains a distinct component for predicting peak broadening related to crystallite microstrain and uses diffraction peak broadening from at least four diffraction peaks as a foundation for calculating crystallite size. The interpretation of crystallite size from diffraction data was based on spherical particles with cubic symmetry. The Williamson-Hall plot was effective in determining the size of the crystallites and the inherent microstrain in the nanoparticle of the microcrystalline structure [58–60]. This approach assumes that the Scherrer equation is followed by the corrected line broadening (β_D) of a Bragg reflection (hkl) arising from the small crystallite size <D>:

$$< D > = \frac{k\lambda}{\beta_D \cos \theta} \tag{2}$$

where <D> is the effective crystallite size normal to the reflecting planes, *k* is the shape factor (~0.9), λ is the X-ray wavelength, and θ_{hhkl} is the Bragg angle.

Additionally, the Williamsom-Hall model takes into account uniform lattice microstrain caused by crystal flaws in the nanocrystals along the crystallographic direction. In other words, it takes into account the isotropic lattice microstrain [61]. The physical broadening of the XRD profile is really impacted by this intrinsic microstrain, and this later-induced peak broadening is stated as:

$$\beta_s = 4\varepsilon \tan \theta \tag{3}$$

Therefore, it is possible to express the overall broadening caused by crystallite size and lattice strain in a specific peak with the (*hkl*) value as:

$$\beta_{hkl} = \beta_D + \beta_s \tag{4}$$

where β_{hkl} is the full width at half of the maximum intensity (FWHM) for the chosen diffraction planes.

$$\beta_{hkl} = \frac{k\lambda}{D}\frac{1}{\cos\theta} + 4\varepsilon\tan\theta \tag{5}$$

When this Equation (5) is re-arranged, we get:

$$\beta_{hkl}\cdot\cos\theta = \frac{k\lambda}{D} + 4\varepsilon\sin\theta \tag{6}$$

Equation (6) is a straight-line equation that takes the crystals' isotropic nature into account. One may determine the lattice microstrain (ε) from the slope straight line of the plot created with $4\sin\theta$ along the x-axis and $\beta_{hkl}.\cos\theta$ along the y-axis for the three samples' oxides and the inverse of average crystallite size (D) from the intercept. For samples of oxides with x = 0, x = 0.4, and x = 1.6, the average particle sizes were determined to be roughly 110, 122, and 131 nm, respectively. The size of a coherently diffracting domain is considered to be the size of a crystallite, which is not always the same as particle size. Meanwhile, the estimated lattice strain values for the samples with x = 0, 0.4, and 1.6 are roughly 0.022, 0.015, and 0.01%, respectively. The atomic arrangement within the crystal lattice is primarily responsible for the lattice contraction or expansion in the crystallites, which is where the lattice microstrain originates. On the other hand, due to size refinement and internal-external stresses that cause lattice strain, numerous defects (point defects such vacancies, stacking faults, grains boundaries, dislocations, etc.) also get generated at the lattice structure. The estimated average crystallite size for the tree samples was approximately 20% less than the theoretical estimates of crystallite size (see Table 1) calculated from the Rietveld refinement.

3.2. Mössbauer Spectrometry

The Mössbauer spectra obtained at 300 and 77 K on the two samples containing Fe are shown in Figure 2. The 300 K spectrum of $Ni_{0.3}Zn_{0.7}Cr_{1.6}Fe_{0.4}O_4$ shows clearly a pure quadrupolar feature, while that of $Ni_{0.3}Zn_{0.7}Cr_{0.4}Fe_{1.6}O_4$ results from a complex hyperfine structure which consists of a quadrupolar component with narrow lines superimposed on a broadened single line feature. The first spectrum can be described by the summation of quadrupolar components, while the second spectrum at 300 K must be described by at least 2 or 3 components: a central quadrupolar doublet, a broadened single line, and possibly a magnetic sextet. At 77 K, the Mössbauer spectra are composed of a magnetic component with broadened lines and a quadrupolar component or a broadened single line. The mean values of isomer shift suggest the presence of exclusively Fe^{3+} species (0.30 and 0.35 for $Ni_{0.3}Zn_{0.7}Cr_{1.6}Fe_{0.4}O_4$ and $Ni_{0.3}Zn_{0.7}Cr_{0.4}Fe_{1.6}O_4$ at 300 K and 0.42 and 0.45, respectively, at 77 K). However, the lack of resolution of the hyperfine structures prevents estimating accurately the proportions of Fe located in the octahedral and tetrahedral sites: it should be necessary to use in-field Mössbauer spectrometry to get such proportions.

These complex hyperfine structures are consistent with a variety of different chemical atomic neighbors, including Ni^{2+}, Zn^{2+}, Cr^{3+}, and Fe^{3+} species which possess different magnetic moments. The highest values of the hyperfine field at Fe sites are a priori the result of a Fe-rich neighboring, the intermediate values of a Ni and Cr-rich neighboring, while the quadrupolar component is assigned to Zn-rich neighboring.
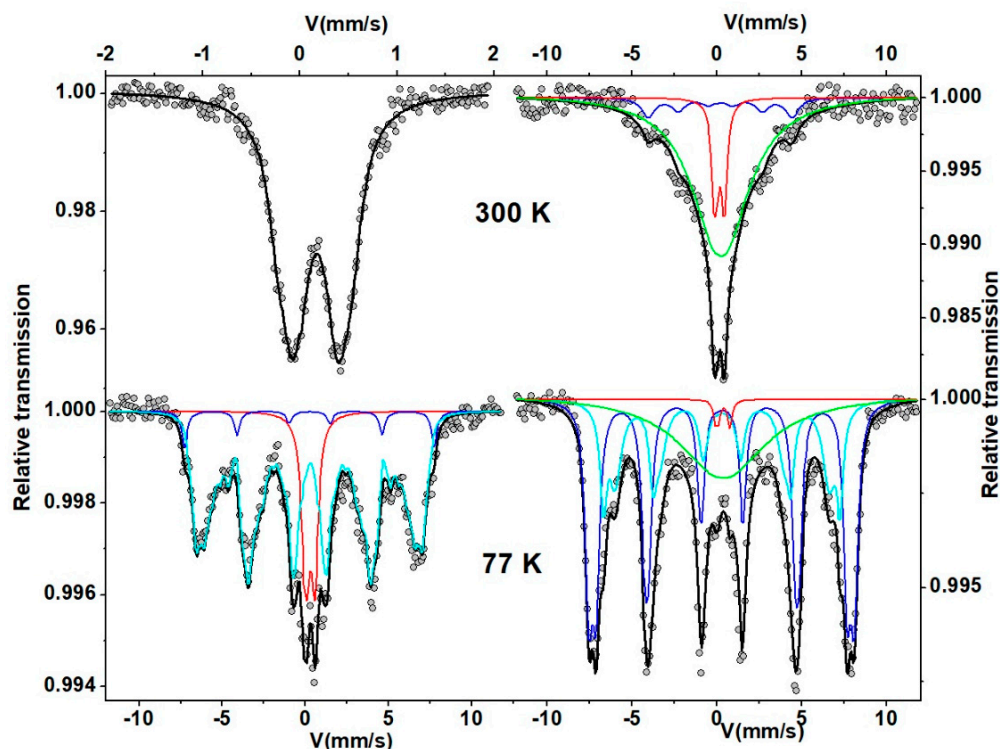
Figure 2. Mössbauer spectra obtained on $Ni_{0.3}Zn_{0.7}Cr_{1.6}Fe_{0.4}O_4$ (**left**) and $Ni_{0.3}Zn_{0.7}Cr_{0.4}Fe_{1.6}O_4$ (**right**) at 300 (**top**) and 77 K (**bottom**): the red, dark blue, cyan and green components correspond to the Zn-rich, Fe-rich, Ni-rich, and Cr-rich neighboring, respectively (see text).

3.3. Morphological Study

Figure 3a–c display the SEM images of $Ni_{0.3}Zn_{0.7}Cr_{2-x}Fe_xO_4$ (x = 0; 0.4; 1.6) ferrite samples at two different magnifications (a–c). As shown, the ferrite samples of $Ni_{0.3}Zn_{0.7}Cr_2O_4$, $Ni_{0.3}Zn_{0.7}Cr_{1.6}Fe_{0.4}O_4$, and $Ni_{0.3}Zn_{0.7}Cr_{0.4}Fe_{1.6}O_4$ have typical particle sizes between 0.5 and 2 µm. These microscopic particles were also dispersed in the material and were dense. It is clear that each particle results from the aggregation of many crystals because the particle sizes determined from SEM images are larger than those estimated using the XRD data. In addition, when the iron proportion increases from 0 to 1.6 at %, the shape of the particles changes from multifaceted to spherical and homogeneous. In addition, magnetic attraction can be the cause of particle adhesion.

3.4. Magnetic Characteristics

A magnetometer (VSM) is used to examine the synthesized materials' magnetic characteristics while they are at room temperature. The M-H curves of the $Ni_{0.3}Zn_{0.7}Cr_{2-x}Fe_xO_4$ (x = 0; 0.4; 1.6) ferrite samples are shown in Figure 4. Table 2 provides the matching saturation magnetization (Ms) and coercivity (Hc) values for various percentages of x. As shown, the maximum value of Ms is found around 0.46 emu/g in the $Ni_{0.3}Zn_{0.7}Cr_2O_4$ sample. While the ferrite samples $Ni_{0.3}Zn_{0.7}Cr_{1.6}Fe_{0.4}O_4$ and $Ni_{0.3}Zn_{0.7}Cr_{0.4}Fe_{1.6}O_4$ exhibit nearly unmeasurable remanence and coercivity with no discernible hysteresis. The magnetization of the samples has been shown to be related to various factors, such as sublattice interactions, spin tilt, the magnitude of the individual moment of the cations, grain size, etc. A strong A-O-B interaction also causes a ferrimagnetic order to form in the spinels. Meanwhile, the presence of chromium in the site (B) reduces the strength of the A-O-B interaction, which can eventually be destroyed [62]. On the other hand, superparamagnetism has this special characteristic [63]. The small value of Ms corresponds to spin canting in the surface layer of nanoparticles. In contrast to local symmetry for those atoms close to the surface layer, which resulted in a decreased Ms in these nanocrystals, the canting

and disorder of the surface layer spins may be caused by broken super-exchange bonds. Additionally, because of the relatively low Zn content (around 0.7), the Zn^{2+} cations in the tetrahedral sites occupy fewer spins in the A sites, decreasing the A-B super-exchange interactions, and the spines of the octahedral sites are unable to maintain collinearity with the tiny tetrahedral spins. Consequently, the Ms looks to be relatively low for x = 0 or null for x = 0.4 and 1.6.
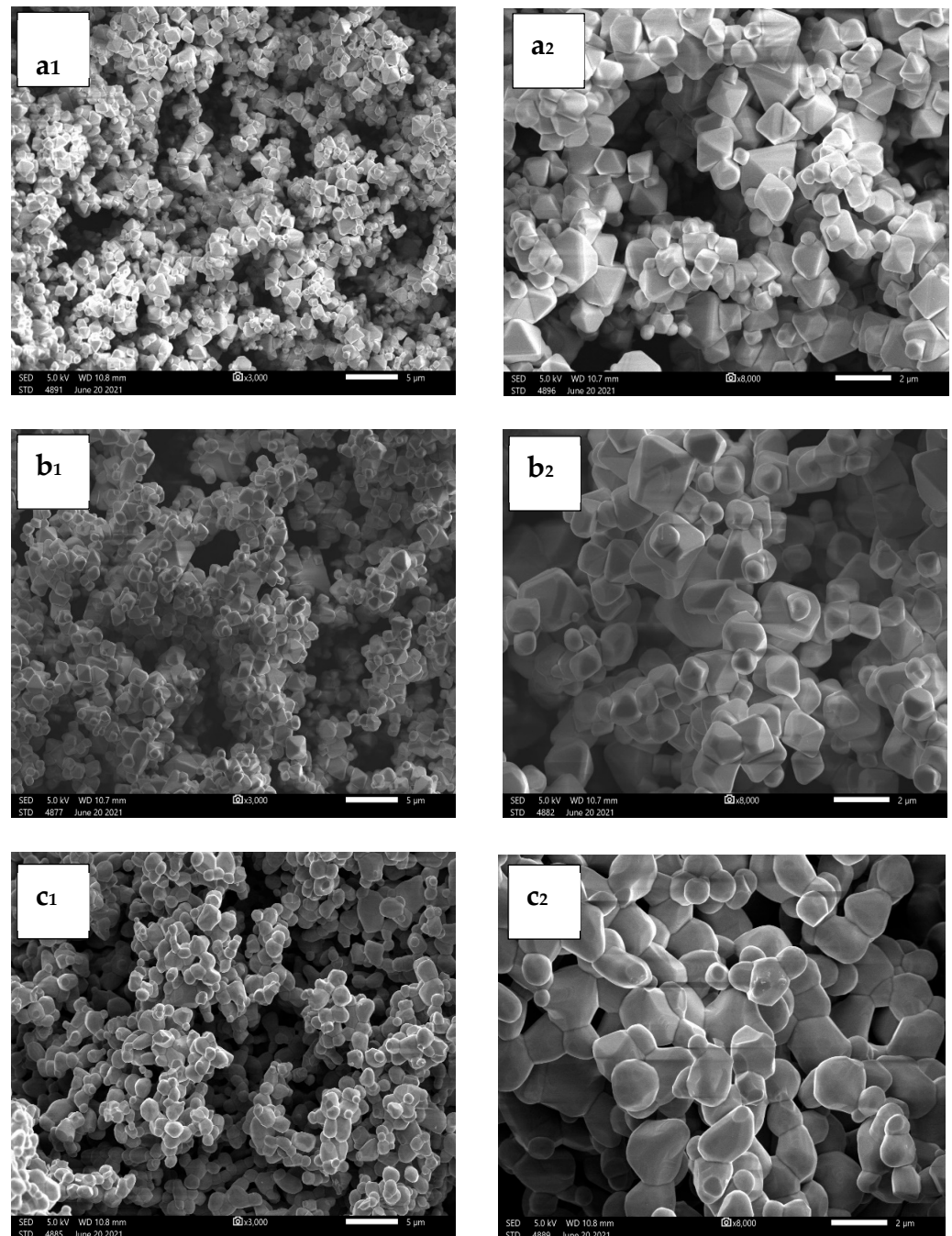

Figure 3. SEM images of the $Ni_{0.3}Zn_{0.7}Cr_{2-x}Fe_xO_4$ (x = 0 (**a**); 0.4 (**b**); 1.6(**c**)) ferrite samples (**left** scale bars: 5 μm, **right** scale bars: 2 μm).
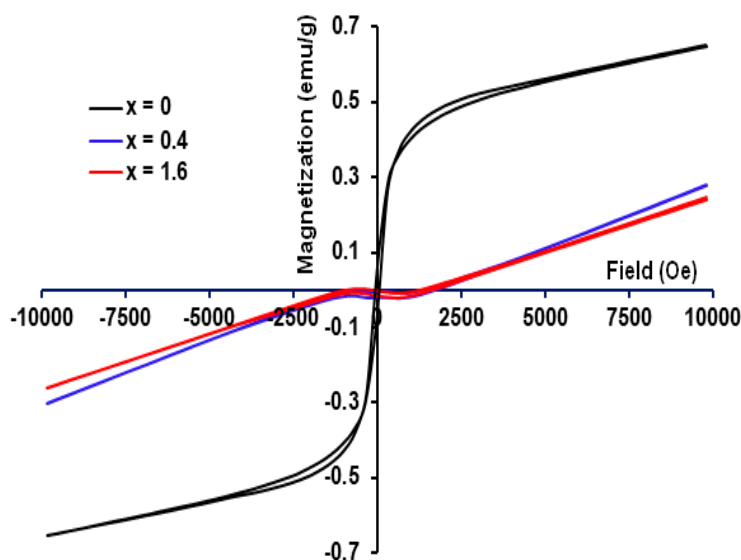
Figure 4. Hysteresis loops of $Ni_{0.3}Zn_{0.7}Cr_{2-x}Fe_xO_4$ (x = 0, 0.4 and 1.6) samples at room temperature.

Table 2. Cation distribution, crystalline size, lattice parameter, saturation magnetization, and coercivity of $Ni_{0.3}Zn_{0.7}Cr_{2-x}Fe_xO_4$ compounds.

x$_{Fe}$	Composition	Cation Distribution	D (nm) ±2	a (Å) ±0.0005	Ms (emu/g)	Hc (Oe) ±5
0	$Ni_{0.3}Zn_{0.7}Cr_2O_4$	$\left(Zn_{0.7}^{2+}Cr_{0.3}^{3+}\right)_A\left[Ni_{0.3}^{2+}Cr_{1.7}^{3+}\right]_B O_4^{2-}$	156	8.3242	0.46	316
0.4	$Ni_{0.3}Zn_{0.7}Cr_{1.6}Fe_{0.4}O_4$	$\left(Zn_{0.7}^{2+}Fe_{0.3}^{3+}\right)_A\left[Ni_{0.3}^{2+}Cr_{1.6}^{3+}Fe_{0.1}^{3+}\right]_B O_4^{2-}$	163	8.3329	--	...
1.6	$Ni_{0.3}Zn_{0.7}Cr_{0.4}Fe_{1.6}O_4$	$\left(Zn_{0.7}^{2+}Fe_{0.3}^{3+}\right)_A\left[Ni_{0.3}^{2+}Cr_{0.4}^{3+}Fe_{1.3}^{3+}\right]_B O_4^{2-}$	172	8.3906	-----	...

The low coercivity value of 316 Oe (Table 2) implies that the $Ni_{0.3}Zn_{0.7}Cr_2O_4$ sample is soft magnetic. This is due to the presence of grain boundaries in the sample, which need less energy to align along the external magnetic field in comparison to domain movement. Previous studies have shown that the presence of the paramagnetic ion Cr^{3+} introduced magnetic dilution into ferrites similar to that produced by non-magnetic substitution, which can induce interesting properties in ferrites. Metal cations can be used to adjust the magnetic characteristics of a system for a specific application.

Based on the Rietveld analysis (Table 1) and the VSM measurements (Figure 3), the absence of the Ni^{2+} ions as ferromagnetic ions and the occupancy of Zn^{2+} ions with zero magnetic moments in all tetrahedral sites—i.e., replacing the entire Fe^{3+} ions in the octahedral sites—are responsible for the small Ms of $Ni_{0.3}Zn_{0.7}Cr_{2-x}Fe_xO_4$. Due to the weakened B-B connection in ferrites and the weak interactions between Fe^{3+} ions in the octahedral sites, the magnetization of the current nanocrystals is low or nonexistent. Additionally, Kodama [64] and Priyadharsini et al. [65] reported that the core-shell model, which explains how the finite size effects of the nanoparticles lead to a canting of spins on their surface and subsequently reduce their magnetizability, can be used to understand the low value of Ms (compared to that of bulk Ni-ferrite (56 emu/g) [66]).

4. Conclusions

In the current study, the sol-gel synthesis process was used to create $Ni_{0.3}Zn_{0.7}Cr_{2-x}Fe_xO_4$ ferrite samples with x = 0, 0.4, and 1.6. The dry gel samples were subsequently heated at temperatures 473 (for 24 h), 773 (for 24 h), 1173 K (for 24 h), and 1448 K (for 48 h) in an air atmosphere. The structure, microstructure, and magnetic characteristics of the

prepared ferrites particles were studied by the use of X-ray diffraction (XRD), scanning electron microscopy (SEM), vibrating sample magnetometer (VSM), and ^{57}Fe Mössbauer spectrometry. All diffraction peaks, as determined by the XRD investigation, were indexed in the cubic *Fd3m* spinel structure with a crystallite size fitted for 140–160 nm.

The proposed cation distributions revealed that Fe^{3+} and Cr^{3+} ions are distributed on both sites, whereas Ni^{2+} ions are distributed on the octahedral B-sites, and Zn^{2+} ions prefer to reside on the tetrahedral A-sites. Based on this distribution the detailed formulas are described as $\left(Zn_{0.7}^{2+}Cr_{0.3}^{3+}\right)_A\left[Ni_{0.3}^{2+}Cr_{1.7}^{3+}\right]_B O_4^{2-}$, $\left(Zn_{0.7}^{2+}Fe_{0.3}^{3+}\right)_A\left[Ni_{0.3}^{2+}Cr_{1.6}^{3+}Fe_{0.1}^{3+}\right]_B O_4^{2-}$, and $\left(Zn_{0.7}^{2+}Fe_{0.3}^{3+}\right)_A\left[Ni_{0.3}^{2+}Cr_{0.4}^{3+}Fe_{1.3}^{3+}\right]_B O_4^{2-}$ for x = 0, 0.4, and 1.6, respectively.

The VSM analyses demonstrate that ferrite samples $Ni_{0.3}Zn_{0.7}Cr_{1.6}Fe_{0.4}O_4$ and $Ni_{0.3}Zn_{0.7}Cr_{0.4}Fe_{1.6}O_4$ possess superparamagnetic properties (with almost immeasurable remanence and coercivity). The phenomenon was justified by the fact that all tetrahedral positions were occupied by Zn^{2+} ions without magnetic moments and were devoid of ferromagnetic Ni^{2+} cations. Further, because of the weak interactions between Fe^{3+} ions in the octahedral locations, the magnetization of the current nanocrystals is low or nonexistent.

The complex hyperfine structures were consistent with a variety of different chemical atomic neighbors, including Ni^{2+}, Zn^{2+}, Cr^{3+}, and Fe^{3+} species, which possess different magnetic moments. At Fe sites, the quadrupolar component was attributed to the Zn-rich neighboring region, while the highest values of the hyperfine field are a priori the result of a Fe-rich neighboring. To overcome the lack of resolution of the hyperfine structures that prevent accurately estimating the proportions of Fe located in the octahedral and tetrahedral sites, it will be necessary to use in-field Mössbauer spectrometry in our future work.

Author Contributions: Conceptualization, A.M. and M.K.; formal analysis, F.A.-T. and J.-M.G.; data curation, A.M.; investigation, A.A. and M.M.A.; writing—original draft preparation, M.K. and F.A.-T.; writing—review and editing, M.K., J.-M.G. and J.-J.S.; supervision, A.M. All authors have read and agreed to the published version of the manuscript.

Data Availability Statement: Data will be requested from the authors.

Conflicts of Interest: The authors declare no conflict of interest.

References

1. Mandal, K.; Mandal, S.P.; Agudo, P.; Pal, M. A study of nanocrystalline (Mn–Zn) ferrite in SiO_2 matrix. *Appl. Surf. Sci.* **2001**, *182*, 386–389. [CrossRef]
2. Yang, H.; Shen, L.; Zhao, L. Magnetic properties of nanocrystalline $Li_{0.5}Fe_{2.1}Cr_{0.4}O_4$ ferrite. *Mater. Lett.* **2003**, *57*, 2455–2459. [CrossRef]
3. Yang, H.; Wang, D.; Wang, Z.; Zhao, M.; Li, M.; Wang, L. A study of the photovoltage properties of nanocrystalline $LiFe_5O_8$. *Mater. Chem. Phys.* **1997**, *48*, 212–215. [CrossRef]
4. Saad, M.M.H.E.; Alsobhi, B.O.; Almeshal, A. Structural, elastic, thermodynamic, electronic, magnetic, thermoelectric and optical investigation of chromate spinels TCr_2O_4 [T = V^{2+}, Mn^{2+}, Fe^{2+}] for optoelectronic applications. *Mater. Chem. Phys.* **2023**, *294*, 127041. [CrossRef]
5. Chen, Q.; Zhang, Z.J. Size-dependent superparamagnetic properties of $MgFe_2O_4$ spinel ferrite nanocrystallites. *J. Appl. Phys.* **1998**, *73*, 3156–3158. [CrossRef]
6. Li, F.; Wang, H.; Wang, L.; Wang, J. Magnetic properties of $ZnFe_2O_4$ nanoparticles produced by a low-temperature solid-state reaction method. *J. Magn. Magn. Mat.* **2007**, *309*, 295–299. [CrossRef]
7. Sun, S.; Zeng, H.; Robinson, D.B.; Raoux, S.; Rice, P.M.; Wang, S.X.; Li, G. Preparation and Reversible Phase Transfer of $CoFe_2O_4$ Nanoparticles. *J. Am. Chem. Soc.* **2004**, *126*, 2782. [CrossRef]
8. Hyeon, T.; Chung, Y.; Park, J.; Lee, S.S.; Kim, Y.W.; Park, B.H. Monodisperse MFe_2O_4 (M = Fe, Co, Mn) Nanoparticles. *J. Phys. Chem. B* **2002**, *106*, 6831. [CrossRef]
9. Pradhan, S.K.; Bid, S.; Gateshki, M.; Petkov, V. Microstructure characterization and cation distribution of nanocrystalline magnesium ferrite prepared by ball milling. *Mater. Chem. Phys.* **2005**, *93*, 224–230. [CrossRef]

10. Sepelak, V.; Becker, K.D. Mössbauer studies in the mechanochemistry of spinel ferrites. *J. Mater. Synth. Process* **2000**, *8*, 155–166. [CrossRef]

11. Roy, S.; Dubenko, I.; Edorh, D.D.; Ali, N. Size-induced variations in structural and magnetic properties of double exchange $La_{0.8}Sr_{0.2}MnO_3-\delta$ nano-ferromagnet. *J. Appl. Phys.* **2004**, *96*, 1202. [CrossRef]

12. McHenry, M.E.; Laughlin, D.E. Nano-scale materials development for future magnetic applications. *Acta Mater.* **2000**, *48*, 223. [CrossRef]

13. Jacob, J.; Abdul Khadar, M. VSM and Mössbauer study of nanostructured hematite. *J. Magn. Magn. Mater.* **2010**, *322*, 614–621. [CrossRef]

14. Kodama, R.H.; Berkowitz, A.E.; McNiff, E.J.; Foner, S. Surface Spin Disorder in $NiFe_2O_4$ Nanoparticles. *Phys. Rev. Lett.* **1996**, *77*, 394. [CrossRef] [PubMed]

15. Chinnasamy, C.N.; Narayanasamy, A.; Ponpandian, N.; Justin Joseyphus, R.; Jayadevan, B.; Tohji, K.; Chattopadhyay, K. Grain size effect on the Néel temperature and magnetic properties of nanocrystalline $NiFe_2O_4$ spinel. *J. Magn. Magn. Mater.* **2002**, *238*, 281. [CrossRef]

16. Shi, Y.; Ding, J. Strong unidirectional anisotropy in mechanically alloyed spinel ferrites. *J. Appl. Phys.* **2001**, *90*, 4078. [CrossRef]

17. Lin, D.; Nunes, A.C.; Majkrzak, C.F.; Berkowitz, A.E. Polarized neutron study of the magnetization density distribution within a $CoFe_2O_4$ colloidal particle II. *J. Magn. Magn. Mater.* **1995**, *145*, 343. [CrossRef]

18. Oliver, S.A.; Harris, V.G.; Hamdeh, H.H.; Ho, J.C. Large zinc cation occupancy of octahedral sites in mechanically activated zinc ferrite powders. *Appl. Phys. Lett.* **2000**, *76*, 2761. [CrossRef]

19. Jiang, J.Z.; Goya, G.F.; Rechenberg, H.R. Magnetic properties of nanostructured $CuFe_2O_4$. *J. Phys. Condens. Matter* **1999**, *11*, 4063. [CrossRef]

20. Abraham, T. Economics of ceramic magnet. *Am. Ceram. Soc. Bull.* **1994**, *73*, 62–65.

21. Seyyed Ebrahimi, S.A.; Azadmanjiri, J. Evaluation of $NiFe_2O_4$ ferrite nanocrystalline powder synthesized by a sol–gel auto-combustion method. *J. Non-Cryst. Solids* **2007**, *353*, 802. [CrossRef]

22. Rashad, M.M.; Fouad, O.A. Synthesis and characterization of nano-sized nickel ferrites from fly ash for catalytic oxidation of CO. *Mater. Chem. Phys.* **2005**, *94*, 365. [CrossRef]

23. Blum, S.L. Microstructure and properties of ferrites. *J. Am. Ceram. Soc.* **1958**, *41*, 489. [CrossRef]

24. Lin, C. Behavior of ferro-or ferrimagnetic very fine particles. *J. Appl. Phys.* **1961**, *32*, S233. [CrossRef]

25. Brook, R.J.; Kingery, W.D. Nickel ferrite thin films: Microstructures and magnetic properties. *J. Appl. Phys.* **1967**, *38*, 3589. [CrossRef]

26. Pradeep, A.; Priyadharsini, P.; Chandrasekaran, G. Production of single phase nano size $NiFe_2O_4$ particles using sol–gel auto combustion route by optimizing the preparation conditions. *Mater. Chem. Phys.* **2008**, *112*, 572. [CrossRef]

27. Nathani, H.; Misra, R.D.K. Surface effects on the magnetic behavior of nanocrystalline nickel ferrites and nickel ferrite-polymer nanocomposites. *Mater. Sci. Eng. B* **2004**, *113*, 228. [CrossRef]

28. George, M.; John, A.M.; Nair, S.S.; Joy, P.A.; Anantharaman, M.R. Finite size effects on the structural and magnetic properties of sol–gel synthesized $NiFe_2O_4$ powders. *J. Magn. Magn. Mater.* **2006**, *302*, 190. [CrossRef]

29. Xianghui, H.; Zhenhua, C. A study of nanocrystalline $NiFe_2O_4$ in a silica matrix. *Mater. Res. Bull.* **2005**, *40*, 105. [CrossRef]

30. Gubbala, S.; Nathani, H.; Koizol, K.; Misra, R.D.K. Magnetic properties of nanocrystalline Ni-Zn, Zn-Mn, Ni-Mn ferrites synthesized by reverse micelle technique. *J. Phys. B* **2004**, *348*, 317–328. [CrossRef]

31. Saafan, S.A.; Meaz, T.M.; El-Ghazzawy, E.H.; El Nimr, M.K.; Ayad, M.M.; Bakr, M. A.C. and D.C. conductivity of NiZn ferrite nanoparticles in wet and dry conditions. *J. Magn. Magn. Mater.* **2010**, *322*, 2369–2374. [CrossRef]

32. Singhal, S.; Chandra, K. Cation distribution and magnetic properties in chromium-substituted nickel ferrites prepared using aerosol route. *J. Solid State Chem.* **2007**, *180*, 296–300. [CrossRef]

33. Tsay, C.Y.; Liu, K.S.; Lin, T.F.; Lin, I.N. Microwave sintering of NiCuZn ferrites and multilayer chip inductors. *J. Magn. Magn. Mater.* **2000**, *209*, 189–192. [CrossRef]

34. Aphesteguy, J.C.; Damiani, A.; DiGiovanni, D.; Jacobo, S.E. Microwave-absorbing characteristics of epoxy resin composite containing nanoparticles of NiZn- and NiCuZn-ferrite. *J. Phys. B* **2009**, *404*, 2713–2716. [CrossRef]

35. Eustace, D.A.; Docherty, F.T.; McComb, D.W.; Craven, A.J. ELNES as a Probe of Magnetic Order in Mixed Oxides. *J. Phys. Conf. Ser.* **2006**, *26*, 165. [CrossRef]

36. Sijo, A.K. Magnetic and structural properties of $CoCr_xFe_{2-x}O_4$ spinels prepared by solution self-combustion method. *Ceram. Int.* **2017**, *43*, 2288–2290. [CrossRef]

37. Raghasudha, M.; Ravinder, D.; Veerasomaiah, P. FTIR Studies and Dielectric Properties of Cr Substituted Cobalt Nano Ferrites Synthesized by Citrate-Gel Method. *Nanosci. Nanotech.* **2013**, *3*, 105–114. [CrossRef]

38. Sijo, A.K.; Dimple, P.D.; Roy, M.; Sudheesh, V.D. Magnetic and dielectric properties of $NiCrFeO_4$ prepared by solution self-combustion method. *Mater. Res. Bull.* **2017**, *94*, 154–159. [CrossRef]

39. Rietveld, H.M. A profile refinement method for nuclear and magnetic structures. *J. Appl. Cryst.* **1969**, *2*, 65. [CrossRef]

40. Teillet, J.; Varret, F. MOSFIT Program, Université du Maine, Le Mans, France. *unpublished*.

41. Chakrabarti, M.; Sanyal, D.; Chakrabarti, A. Preparation of $Zn_{(1-x)}Cd_xFe_2O_4$ (x = 0.0, 0.1, 0.3, 0.5, 0.7 and 1.0) ferrite samples and their characterization by Mössbauer and positron annihilation techniques. *J. Phys. Condens. Matter* **2007**, *19*, 1. [CrossRef]

42. Patange, S.M.; Shirsath, S.E.; Jadhav, S.S.; Jadhav, K.M. Cation distribution study of nanocrystalline NiFe$_{2-x}$Cr$_x$O$_4$ ferrite by XRD, magnetization and Mössbauer spectroscopy. *Phys. Status Solidi A* **2012**, *209*, 347. [CrossRef]

43. Gismelseed, A.M.; Yousif, A.A. Mössbauer study of chromium-substituted nickel ferrites. *Phys. B* **2005**, *370*, 215. [CrossRef]

44. Anwar, M.S.; Ahmed, F.; Koo, B.H. Enhanced relative cooling power of Ni$_{1-x}$Zn$_x$Fe$_2$O$_4$ (0.0 ≤ x ≤ 0.7) ferrites. *Acta Mater.* **2014**, *71*, 100. [CrossRef]

45. Hakim, M.A.; Nath, S.K.; Sikder, S.S.; Maria, K.H. Cation distribution and electromagnetic properties of spinel type Ni–Cd ferrites. *J. Phys. Chem. Solids* **2013**, *74*, 1316. [CrossRef]

46. Lohar, K.S.; Patange, S.M.; Mane, M.L.; Shirsath, S.E. Cation distribution investigation and characterizations of Ni$_{1-x}$Cd$_x$Fe$_2$O$_4$ nanoparticles synthesized by citrate gel process. *J. Mol. Struct.* **2013**, *1032*, 105–110. [CrossRef]

47. Khalaf, K.A.; Al Rawas, A.D.; Gismelssed, A.M.; Al Jamel, A.; Al Ani, S.K.; Shongwe, M.S.; Al Riyami, K.O.; Al Alawi, S.R. Influence of Cr substitution on Debye-Waller factor and related structural parameters of ZnFe$_{2-x}$Cr$_x$O$_4$ spinels. *J. Alloys Compd.* **2017**, *701*, 474–486. [CrossRef]

48. Shannon, R.D. Revised effective ionic radii and systematic studies of interatomic distances in halides and chalcogenides. Acta crystallographica section A: Crystal physics, diffraction, theoretical and general crystallography. *Acta Cryst.* **1976**, *32*, 751–767. [CrossRef]

49. Hcini, S.; Kouki, N.; Omri, A.; Dhahri, A.; Bouazizi, M.L. Effect of sintering temperature on structural, magnetic, magnetocaloric and critical behaviors of Ni-Cd-Zn ferrites prepared using sol-gel method. *J. Magn. Magn. Mater.* **2018**, *464*, 91–102. [CrossRef]

50. Kouki, N.; Hcini, S.; Boudard, M.; Aldawas, R.; Dhahri, A. Microstructural analysis, magnetic properties, magnetocaloric effect, and critical behaviors of Ni$_{0.6}$Cd$_{0.2}$Cu$_{0.2}$Fe$_2$O$_4$ ferrites prepared using the sol–gel method under different sintering temperatures. *RSC Adv.* **2019**, *9*, 1990–2001. [CrossRef]

51. Kumar, G.; Kotnala, R.K.; Shah, J.; Kumar, V.; Kumar, A.; Dhiman, P.; Singh, M. Cation distribution: A key to ascertain the magnetic interactions in a cobalt substituted Mg–Mn nanoferrite matrix. *Phys. Chem. Chem. Phys.* **2017**, *19*, 16669. [CrossRef]

52. Sharma, R.; Thakur, P.; Kumar, M.; Thakur, J.N.; Negi, N.S.; Sharma, P.; Sharma, V. Improvement in magnetic behaviour of cobalt doped magnesium zinc nano-ferrites via co-precipitation route. *J. Alloys Compd.* **2016**, *684*, 569–581. [CrossRef]

53. Mhadhbi, M.; Khitouni, M.; Azabou, M.; Kolsi, A. Characterization of Al and Fe nanosized powders synthesized by high energy mechanical milling. *Mater. Charact.* **2008**, *59*, 944–950. [CrossRef]

54. Khitouni, M.; Kolsi, A.W.; Njah, N. The effect of boron additions on the disordering and crystallite refinement of Ni3Al powders during mechanical milling. *Ann. Chim. Sci. Mat.* **2003**, *28*, 17–29. [CrossRef]

55. Nath, D.; Singh, F.; Das, R. X-ray diffraction analysis by Williamson-Hall, Halder-Wagner and size-strain plot methods of CdSe nanoparticles- a comparative study. *Mater. Chem. Phys.* **2020**, *239*, 122021. [CrossRef]

56. Williamson, G.K.; Hall, W.H. X-ray line broadening from filed aluminum and wolfram. *Acta Metall.* **1953**, *1*, 22–31. [CrossRef]

57. Klug, H.P.; Alexander, L.E. *X-ray Diffraction Procedure for Polycrystalline and Amorphous Materials*; Wiley: New York, NY, USA, 1974.

58. Bindu, P.; Thomas, S. Estimation of lattice strain in ZnO nanoparticles: X-ray peak profile analysis. *J. Theor. Appl. Phys.* **2014**, *8*, 123–134. [CrossRef]

59. Chenari, H.M.; Seibel, C.; Hauschild, D.; Reinert, F.; Abdollahian, H. Titanium dioxide nanoparticles: Synthesis, X-ray line analysis, and chemical composition study. *Mater. Res.* **2016**, *19*, 1319–1323. [CrossRef]

60. Kumar, S.; Mote, V.; Prakash, R.; Kumar, V. X-ray analysis of α-Al$_2$O$_3$ particles by Williamson–Hall methods. *Mater. Focus* **2016**, *5*, 545–549. [CrossRef]

61. Hall, W.H. X-ray line broadening in metals. *Proc. Phys. Soc. Sect.* **1949**, *62*, 741–743. [CrossRef]

62. Hcini, S.; Boudard, M.; Zemni, S.; Oumezzine, M. Critical behavior of Nd$_{0.67}$Ba$_{0.33}$Mn$_{1-x}$Fe$_x$O$_3$ (x = 0 and 0.02) manganites. *Ceram. Int.* **2015**, *41*, 2042–2049. [CrossRef]

63. Leslie-Pelecky, D.L.; Rieke, R.D. Magnetic properties of nanostructured materials. *Chem. Mater.* **1996**, *8*, 1770–1783. [CrossRef]

64. Kodama, R.H. Magnetic Nanoparticle. *J. Magn. Magn. Mater.* **1999**, *200*, 359–372. [CrossRef]

65. Priyadharsini, P.; Pradeep, A.; Rao, P.S.; Chandrasekaran, G. Structural, spectroscopic and magnetic study of nanocrystalline Ni–Zn ferrites. *Mater. Chem. Phys.* **2009**, *116*, 207–213. [CrossRef]

66. Maaz, K.; Karim, S.; Mumtaz, A.; Hasanain, S.K.; Liu, J.; Duan, J.L. Synthesis and magnetic characterization of nickel ferrite nanoparticles prepared by co-precipitation route. *J. Magn. Magn. Mater.* **2009**, *321*, 1838–1842. [CrossRef]